13th International Symposium on Particle Image Velocimetry – ISPIV 2019
Munich, Germany, July 22-24, 2019

Assessment of Uncertainty Quantification methods for density estimation from Background Oriented Schlieren (BOS) measurements

Lalit K. Rajendran[1], Sayantan Bhattacharya[2], Jiacheng Zhang[2], Sally P.M. Bane[1] and Pavlos P. Vlachos[2]*

[1]Purdue University, School of Aeronautics and Astronautics, West Lafayette, USA.

[2] Purdue University, School of Mechanical Engineering, West Lafayette, USA.

*pvlachos@purdue.edu

Abstract

We present an uncertainty quantification methodology for density estimation from Background Oriented Schlieren (BOS) measurements, in order to provide local, instantaneous a-posteriori uncertainty bounds on each density measurement in the field of view. We apply displacement uncertainty quantification algorithms adopted from cross-correlation based Particle Image Velocimetry (PIV) to estimate the uncertainty in the dot pattern displacements obtained from cross-correlation for BOS and develop a methodology to propagate the displacement uncertainty through the density integration via the Poisson solver to density estimation uncertainty. We test the method using synthetic images of a Gaussian density field, and experimental images of supersonic flow over a wedge.

1. Introduction

Background Oriented Schlieren (BOS) is a type of quantitative schlieren diagnostic technique, where the apparent distortion of a dot pattern viewed through a medium with refractive index gradients is measured using cross-correlation, tracking or optical flow based algorithms to estimate the density gradients in the medium (Dalziel, Hughes, & Sutherland, 2000; Meier, 2002; Raffel, Richard, & Meier, 2000; Richard & Raffel, 2001). The density gradients can be integrated spatially to obtain the 2D density field (Venkatakrishnan & Meier, 2004). Owing to the simple setup and ease of use, BOS has been applied widely in laboratory scale as well as in large scale and rugged industrial facilities, and is becoming the preferred method of density measurement in fluid flows (Elsinga, Van Oudheusden, Scarano, & Watt, 2004; Kirmse et al., 2011; Mizukaki, Wakabayashi, Matsumura, & Nakayama, 2014; Raffel, 2015; Ramanah, Raghunath, Mee, Rösgen, & Jacobs, 2007; Richard, Raffel, Rein, Kompenhans, & Meier, 2002; Venkatakrishnan, 2005; Venkatakrishnan & Suriyanarayanan, 2009).

In addition to being used to investigate flow physics, BOS measurements are also beginning to be used in conjunction with Computational Fluid Dynamics (CFD) codes for model validation and design (Kirmse et al., 2011; Ramanah et al., 2007; Singh et al., 2019; Sommersel, Bjerketvedt, Christensen, Krest, & Vaagsaether, 2008; Sourgen, Haertig, & Rey, 2004). However, there currently exists no comprehensive framework for quantifying the associated uncertainties in the density estimation to guide these efforts. The BOS measurement involves a complex measurement chain and is subject to several sources of uncertainties ranging from the dot pattern parameters (dot size, dot

density), non-uniform illumination, vibrations, blurring/out-of-focus effects, non-linearities and small scale fluctuations in the flow field, uncertainties in measurement of the optical layout, as well as the processing and post processing methodologies used to calculate the density from the image displacements. As a result, the uncertainty on the final density measurement is a high-dimensional, coupled, non-linear and non-trivial function of several parameters, and can vary widely across the field of view and across a time series of measurements. Therefore, a method for estimating and reporting uncertainties on BOS measurement is needed.

For a measurement u, the uncertainty σ_u is defined as the interval around the measurement in which the true value u_0, and by extension the true error δ_{u_0}, is believed to exist (Coleman & Steele, 2009). The standard uncertainty is defined as the range of measurement values one standard deviation σ about the true value, for an arbitrary parent population. The expanded uncertainty is defined for an assumed parent distribution for the error, and is specified using a confidence interval at a defined percentage, and a coverage factor t_{CI}, to indicate that the true value/error lies in an interval $\sigma_u = t_{CI}\sigma$ around the measurement for the pre-defined percentage of samples drawn from the parent distribution. For example, if the errors are drawn from a Gaussian distribution, the expanded uncertainty at 68% confidence interval is equal to the standard uncertainty ($\sigma_u = \sigma$), and the expanded uncertainty at 95% confidence interval is equal to approximately twice the standard uncertainty ($\sigma_u = 1.96\sigma$). The aim of this paper is to propose and implement an uncertainty quantification methodology to provide a-posteriori, local, instantaneous uncertainty bounds for each density measurement in the field of view for a BOS experiment, and the standard uncertainty is reported throughout this paper.

In the related field of Particle Image Velocimetry (PIV) (Adrian, 2005; Adrian & Westerweel, 2011; Raffel, Willert, Wereley, & Kompenhans, 2013; Westerweel, Elsinga, & Adrian, 2013), there have been widespread efforts in the past decade to develop a-posteriori uncertainty quantification methodologies that allow the estimation and reporting of instantaneous uncertainty on the particle displacement across the field of view (Christensen & Scarano, 2015; Sciacchitano, 2019), as well as to perform comparative assessment of the existing methods on synthetic and experimental images (Boomsma, Bhattacharya, Troolin, Pothos, & Vlachos, 2016; Sciacchitano et al., 2015). PIV also has a complex measurement chain and has many error sources that can contribute to the overall uncertainty. As the displacement estimation in BOS is similar to the displacement estimation in PIV, in that both primarily use multigrid cross-correlation algorithms with a subpixel fit, the PIV based displacement uncertainty methods will be utilized as a part of the present methodology.

There have been many displacement uncertainty estimation methods proposed for 2D planar PIV and they can be broadly divided into indirect and direct methods. Indirect methods predict the displacement uncertainty by calibrating the variation of uncertainty to various image parameters and signal to noise ratio metrics, where the calibration is obtained using Monte-Carlo simulations with synthetic images. For a given experiment, the metric is computed based on the measured data and the calibration function is used to estimate the uncertainty bounds, similar to an instrument calibration procedure. On the other hand, Direct methods estimate uncertainty directly from the properties of the image or correlation plane and do not require any calibration. In two independent comparative assessment of the methods, Sciacchitano et. al. (Sciacchitano et al., 2015) and Boomsma et. al. (Boomsma et al., 2016) found the direct methods to be overall more sensitive to variations in the random error, though Boomsma et. al. (Boomsma et al., 2016) found the direct

methods to underpredict the standard uncertainty in some cases. Since the indirect methods rely on calibration only the direct methods will be considered in this work.

Examples of direct uncertainty estimation methods include the Image Matching (IM) method proposed by Sciacchitano et. al. (Sciacchitano, Wieneke, & Scarano, 2013), Correlation Statistics (CS) method proposed by Wieneke (Wieneke, 2015) and the Moment of Correlation (MC) proposed by Bhattacharya et. al. (Bhattacharya, Charonko, & Vlachos, 2018). Image Matching (IM)/Particle Disparity (PD) proposed by Sciacchitano et. al. (Sciacchitano et al., 2013), estimates the uncertainty in the displacement using a statistical analysis of the disparity between the measured positions of particles/dots in the two frames after a converged iterative deformation interrogation procedure (Scarano, 2002; Scarano & Riethmuller, 2000). Correlation Statistics (CS) proposed by Wieneke (Wieneke, 2015), uses the asymmetry of the correlation peak at the end of a converged window deformation procedure as a measure of the correlation error and the standard deviation of the error is propagated through the subpixel estimator to estimate the displacement uncertainty. Moment of Correlation (MC) proposed by Bhattacharya et. al. (Bhattacharya et al., 2018) predicts the uncertainty from the moment of the of the Generalized Cross Correlation (GCC) defined as the the inverse Fourier transform of the phase of the complex cross-correlation plane (Wernet, 2005)(Eckstein, Charonko, & Vlachos, 2008; Eckstein & Vlachos, 2009b).

There have also been methodologies proposed to extend the uncertainties in the 2D displacement fields to calculation of displacement derived quantities. Wilson and Smith (Wilson & Smith, 2013) extended the displacement uncertainties to estimate uncertainties in mean and fluctuating statistics. Sciacchitano and Wieneke (Sciacchitano & Wieneke, 2016) provided a framework for calculation of uncertainties for displacement gradient based quantities such as the vorticity. Bhattacharya et. al. (Bhattacharya, Charonko, & Vlachos, 2017) proposed a methodology for Stereo-PIV uncertainty quantification by accounting for uncertainties introduced in the calibration and self-calibration process. Azilji et. al. (Azijli, Sciacchitano, Ragni, Palha, & Dwight, 2016) proposed a methodology based on a Bayesian framework to calculate the uncertainties for PIV based pressure measurement in a three-dimensional flow field. A similar approach will also be taken in this paper to propagate displacement uncertainties through the calculation of the density gradients and the density integration procedure, except that here the 2D displacement uncertainties will be calculated from the direct methods.

In this paper we propose and implement a comprehensive framework to model and propagate uncertainties from displacement measurements in a BOS experiment on to the final density measurement. To do this, we use ideas and methodologies from Particle Image Velocimetry (PIV) uncertainty quantification efforts to model the uncertainty in image displacements and propagate these uncertainties through the BOS measurement chain including the density gradient integration and density reconstruction. We test both the PIV displacement uncertainty schemes as well as the uncertainty propagation framework with synthetic and experimental BOS images. The contribution of this paper is an accurate and practical way of estimating uncertainties for BOS experiments.

2. Methodology

The proposed uncertainty quantification methodology closely follows the BOS measurement chain and is shown in Figure 1. First, the raw image pairs and processed displacement fields are used along with PIV based uncertainty estimation methods to calculate the local, instantaneous

uncertainty on each displacement vector. This uncertainty is primarily dependent on image and flow-based parameters. Following this, the details of the optical layout such as the magnification and the distance between the dot pattern and the density gradients is used to estimate the uncertainty in the projected density gradient field.

In BOS experiments the projected density gradient field is related to the apparent displacement of the dot pattern by (1)

$$\nabla\rho_p = \int \nabla\rho \, dz = \frac{\Delta\vec{x}}{Z_D M} \frac{n_0}{K} \tag{1}$$

where $\Delta\vec{x}$ is the displacement, M is the magnification of the dot pattern, Z_D is the distance between the dot pattern and the mid-point of the density gradient field, n_0 is the ambient refractive index, K is the Gladstone-Dale constant (=0.225 cm^3/g for air) and $\rho_p = \int \rho \, dz$ is the projected density field. Similarly, the uncertainty in the projected density gradient field can be expressed by (2)

$$\sigma_{\nabla\rho_p} = \frac{\sigma_{\Delta\vec{x}}}{Z_D M} \frac{n_0}{K} \tag{2}$$

where $\sigma_{\Delta\vec{x}}$ is the displacement uncertainty and $\sigma_{\nabla\rho_p}$ is the uncertainty in the projected density gradient field? It should be noted that some of the experimental parameters occurring in the above equations can also have their own uncertainties such as the magnification M and the distance Z_D. However, they will be assumed to be known and constant in this work, as the main focus is on propagating the displacement-based uncertainties. Further, any uncertainties in this quantities, can be handled in a straightforward manner using the Taylor series propagation model (Coleman & Steele, 2009).

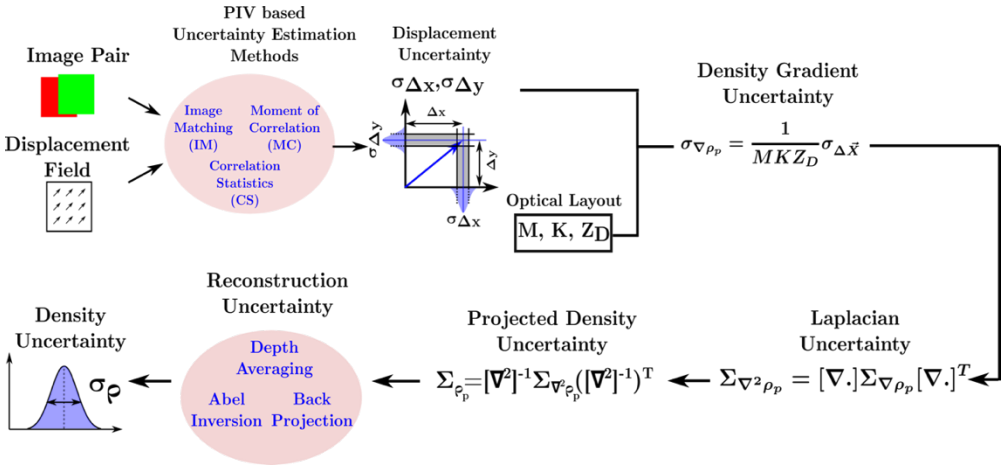

Figure 1. Proposed uncertainty quantification methodology for BOS measurements.

The next step in BOS experiments is to use a finite difference scheme to calculate the Laplacian of the projected density followed by 2D integration by solving the Poisson equation to calculate the projected density field, as shown in (3)

$$\frac{\partial^2\rho_p}{\partial x^2} + \frac{\partial^2\rho_p}{\partial y^2} = S \tag{3}$$

where S denotes the source term that is set to be the Laplacian of the calculated projected density field. The Poisson equation is then discretized into a system of linear equations using finite difference schemes and solved using appropriate boundary conditions (Dirichlet/Neumann) depending on the knowledge of the flow field.

The discretization and solution procedure are as follows. The source term S is calculated from the projected density gradients using a finite difference operator, and is given by

$$\bar{\bar{S}} = \bar{\bar{\nabla}}_x \overline{\frac{\partial \rho_p}{\partial x}} + \bar{\bar{\nabla}}_y \overline{\frac{\partial \rho_p}{\partial y}} \tag{4}$$

where $\bar{\bar{\nabla}}_x, \bar{\bar{\nabla}}_y$ are the mapping matrices (2D arrays represented by a double overbar) that depend on the finite difference scheme, and $\overline{\frac{\partial \rho_p}{\partial x}}, \overline{\frac{\partial \rho_p}{\partial y}}$ are the density gradients (1D arrays represented by a single overbar). A second order central difference discretization scheme is used for the results reported in this paper.

The source term is combined with points on the boundary to create an augmented matrix $\bar{\bar{R}}$, given by

$$\begin{aligned} \bar{\bar{R}} &= \bar{\bar{\nabla}}_x \overline{\frac{\partial \rho_p}{\partial x}} + \bar{\bar{\nabla}}_y \overline{\frac{\partial \rho_p}{\partial y}} + \frac{1}{h^2} \bar{\bar{L}} \bar{\rho}_{p,L} \\ &= \bar{\bar{S}} + \bar{\bar{S}}_L \end{aligned} \tag{5}$$

where $\bar{L}$ is a label matrix (2D array) specifying points on the boundary, and h is the grid spacing.

The projected density is calculated by multiplying the augmented matrix with the augmented Laplacian operator

$$\rho_p = \begin{bmatrix} \bar{\bar{\Delta}} & 0 \\ 0 & \frac{\bar{\bar{L}}}{h^2} \end{bmatrix}^{-1} \begin{bmatrix} \bar{\bar{S}} \\ \bar{\bar{S}}_L \end{bmatrix} \tag{6}$$

where $\bar{\bar{\Delta}}$ is the Laplacian operator for the interior points corresponding to the finite difference schemes used to calculate the Laplacian ($\bar{\bar{\Delta}} = \bar{\bar{\nabla}}_x \bar{\bar{\nabla}}_x{}^T + \bar{\bar{\nabla}}_y \bar{\bar{\nabla}}_y{}^T$).

The uncertainty calculations are performed in a similar manner by propagating the covariances through the finite difference operators. The covariance in the augmented source term is given by

$$\begin{aligned} \bar{\bar{\Sigma}}_R &= \bar{\bar{\nabla}}_x \bar{\bar{\Sigma}}_{\frac{\partial \rho_p}{\partial x}} \bar{\bar{\nabla}}_x^T + \bar{\bar{\nabla}}_y \bar{\bar{\Sigma}}_{\frac{\partial \rho_p}{\partial y}} \bar{\bar{\nabla}}_y^T + \frac{1}{h^2} \bar{\bar{L}} \bar{\bar{\Sigma}}_{\rho_{p_L}} \frac{1}{h^2} \bar{\bar{L}}^T \\ &= \bar{\bar{\Sigma}}_S + \bar{\bar{\Sigma}}_{S_L} \end{aligned} \tag{7}$$

and the covariance in the density is calculated using,

$$\bar{\bar{\Sigma}}_{\rho_p} = \begin{bmatrix} \bar{\bar{\Delta}} & 0 \\ 0 & \frac{\bar{\bar{L}}}{h^2} \end{bmatrix}^{-1} \begin{bmatrix} \bar{\bar{\Sigma}}_S \\ \bar{\bar{\Sigma}}_{S_L} \end{bmatrix} \left(\begin{bmatrix} \bar{\bar{\Delta}} & 0 \\ 0 & \frac{\bar{\bar{L}}}{h^2} \end{bmatrix}^{-1} \right)^T \quad . \tag{8}$$

Finally, the uncertainty in the density is calculated from the square root of the density covariance matrix. All linear operators in the solution procedure are modeled as sparse matrices to increase computational speed. In this manner, the uncertainty in the density field accounts for the choice of the finite difference scheme and the boundary conditions used to calculate the corresponding density field.

Following this, the next step is to calculate the 2D density field either by depth averaging (dividing the projected density field by the thickness of the density gradient field) if the extent of the density field is known, or through an Abel inversion or Filtered Back Projection (FBP) procedure if the flow field is axisymmetric. While each reconstruction procedure can create a different amplification of the uncertainty, only the depth averaged reconstruction approach will be considered in this paper. For situations which involve the use of Abel inversion, the uncertainty can again be propagated through a matrix representation of the Abel inversion procedure, because all the Abel inversion schemes can be represented by linear operators both for interferometric and deflectometric cases (Dasch, 1992; Kolhe & Agrawal, 2009). The final result at the end of all such reconstruction procedures is an estimate of the instantaneous density uncertainty for *each individual grid point*.

In the following sections we test the uncertainty quantification methodology and assess the performance of the various PIV displacement uncertainty schemes and the propagation framework for synthetic and experimental BOS images.

3. Analysis with synthetic images

The error analysis is performed using synthetic BOS images rendered using a ray-tracing based image generation methodology where light rays emerged from the dot pattern are traced through the density gradient field and the optical components of the experimental setup up to the camera sensor to render the final image. This methodology has been validated using analytical solutions for known density field and the rendered images display realistic features of typical BOS experimental setups such as optical aberrations and blurring due to non-linearities in the density field (Rajendran, Bane, & Vlachos, 2019).

The density field chosen for the error analysis is a Gaussian density field, described by Equation (9),

$$\rho(X,Y) = \rho_0 + \Delta\rho_0 \exp - \frac{(X - X_0)^2 + (Y - Y_0)^2}{2\sigma_0^2} \tag{9}$$

where ρ_0 is the ambient density, $\Delta\rho_0$ is the peak density difference and σ_0 is the standard deviation of the Gaussian field.

This field was chosen because it contains significant displacement gradients to test the displacement uncertainty schemes and the density integration procedure, but is smooth everywhere. For the simulations reported in this paper, ρ_0 was set to be 1.225 kg/m^3, $\Delta\rho_0$ was set to be 0.3 kg/m^3, and σ_0 was set to be 1/4th of the field of view (= 2.41 mm). The dimensions of the density gradient field

were 10 x 10 x 10 mm, and it was located at a distance of 0.25 m from the dot pattern. The optical layout used to image the dot pattern and the density field consisted of a 105 mm lens at a distance of 0.5 m from the dot pattern to provide a magnification of about 40 μm/pix. A 2D slice of the three-dimensional density field is shown in Figure 2(a), and the corresponding light ray displacements are shown in Figure 2(b). A three-dimensional volume was created using the same slice stacked along the Z direction (out of plane) to account for the depth averaging limitation of BOS experiments.

(a) (b)

Figure 2. (a) 2D slice of the density field used to render the synthetic BOS images, and (b) the corresponding displacement field.

The images were rendered with a dot size of 3 pix. under diffraction limited imaging, with about 20 dots per 32x32 window. The rendered images were corrupted with noise drawn randomly from a zero-mean Gaussian distribution with a standard deviation of 5% of the peak image intensity. A thousand image pairs were rendered in total to create sufficient statistics for the analysis.

The images were processed using a standard cross-correlation procedure for two passes in an iterative window deformation framework (Scarano, 2002; Scarano & Riethmuller, 2000) with continuous window offset (Gui & Wereley, 2002; Scarano & Riethmuller, 1999; Westerweel, Dabiri, & Gharib, 1997). The window resolution was 32x32 pix. for both passes which corresponds to a 64x64 pix window size, and apodized using a 50% Gaussian window to minimize edge discontinuities, spectral leakage and wraparound aliasing (Eckstein & Vlachos, 2009a). The window overlap was set to 0% (grid resolution = 32x32 pix.) for the analysis to avoid introducing covariance on adjacent displacement vectors from the cross-correlation process, as accounting for this covariance in an automatic calibration-free manner is still a subject of ongoing research (Sciacchitano & Wieneke, 2016). The results of the first pass were validated using the Universal Outlier Detection (UOD) method (Westerweel & Scarano, 2005), while the results of the second pass were not validated. The displacement uncertainties were calculated using the Image Matching (IM), Correlation Statistics (CS) and Moment of Correlation (MC) methods. For the IM and MC methods, the processing and uncertainty calculation was performed using an open source code PRANA (https://github.com/aether-lab/prana/). For CS, the processing and uncertainty calculation was performed with DAVIS 10.0.5 by LaVision. A sample instantaneous displacement field along with the corresponding uncertainty field is shown in Figure 3(a) for results from Prana processing and uncertainties from IM and MC, and in Figure 3(b) for results from Davis processing and uncertainties from CS.

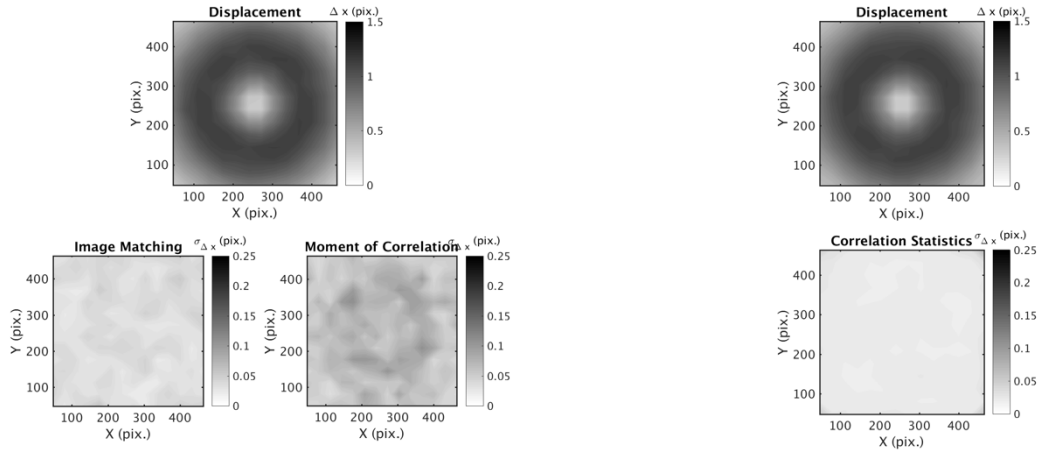

(a) (b)

Figure 3. Sample instantaneous displacement and uncertainty fields for (a) Prana, IM, MC and (b) Davis, CS.

For the error analysis, the displacements obtained from the cross-correlation analysis were compared with the light ray displacements from the ray tracing based image generation procedure to calculate an error for each vector. As the final locations of the light rays will be randomly scattered on the image sensor, an interpolation procedure was performed using a natural neighbor interpolation based on Voronoi tessellations (Sibson, 1981) to calculate the corresponding true displacement for each vector. Finally, the errors corresponding to all vectors from all image pairs were combined to build a probability density function (PDF) for the error distribution and the corresponding error statistics such as the bias error, the random error and the total error were calculated. As each image pair yielded 256 vectors with the above processing procedure, with a total of 1000 images, we have 256000 vectors to calculate the statistics. The error statistics were split into three main components, the bias/systematic error, the random error, and the total error, and they are defined as,

$$\begin{aligned} \delta_{bias} &= E(u - u_{true}) \\ \delta_{random} &= \sqrt{E((u - u_{mean})^2)} \\ \delta_{total} &= \sqrt{E((u - u_{true})^2)} = \sqrt{\delta_{bias}^2 + \delta_{random}^2} \end{aligned} \quad \textbf{(10)}$$

where δ represents the error statistic, u is the measurement, u_{true} is the ground truth, and u_{mean} is the average of the measurements.

The displacement uncertainty estimates from the three direct schemes were compared to the random error from the analysis to assess the performance of these PIV based schemes for synthetic BOS images. The spatial distribution of the error statistics as well as the displacement uncertainties are shown in Figure 4 for Prana-IM-MC processing and for Davis-CS processing. Overall it can be seen that the error statistics are fairly uniform throughout the field of view, with negligible bias error from both processing software programs, and Davis results in a slightly higher error near the center of the FOV. For the spatial variation of the displacement uncertainty, both IM and CS methods

give nearly uniform uncertainties for all vectors in the field of view on the same order of their respective random errors, but MC results in an overprediction of the uncertainty in comparison to the corresponding random error distribution from Prana, especially in regions with higher displacement gradients. One reason for this overprediction could be the small window size used in this work (= 32x32 pix.) as MC is known to overpredict the uncertainty for smaller interrogation windows (Bhattacharya et al., 2018). Further, the presence of displacement gradients can stretch the correlation peak, and amplify the uncertainty prediction. While such a correction is performed in MC, the current formulation accounts only for shear gradients (dU/dy, dV/dx). However, this Gaussian field also features strong axial gradients (dU/dx, dV/dy), that have not been accounted for in the present formulation of the MC method. This might be responsible for the ring of high uncertainty values observed in the ensemble averaged field.

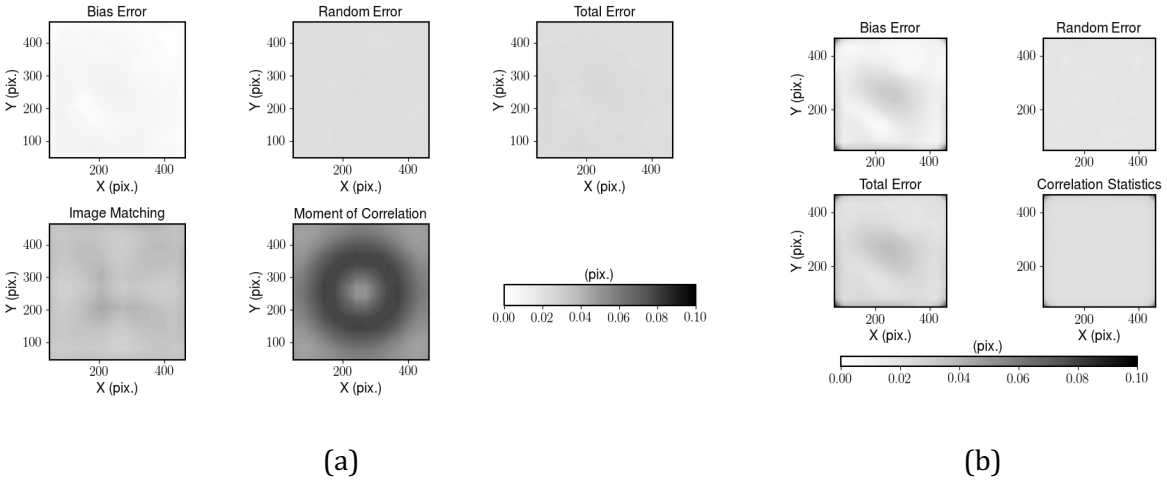

Figure 4. Comparison of displacement error statistics and ensemble averaged displacement uncertainties from (a) Prana, IM and MC, and (b) Davis, CS.

The probability density functions of the errors and uncertainties for results from both software programs are shown in Figure 5, along with dashed lines indicating the RMS values of the random error, and the RMS values of the corresponding uncertainty schemes. The results for Prana-IM-MC are shown in Figure 5 (a), and the results for Davis-CS is shown in Figure 5 (b). It is expected that for a correct uncertainty prediction, the RMS of the random error should coincide with the RMS of the uncertainty distribution (Sciacchitano et al., 2015). From the figures it can be first seen that all three displacement uncertainty schemes overpredict their corresponding random error, but the RMS of the uncertainty from CS comes closest to the RMS of the random error in Figure 5 (b), followed by IM and then MC. Further, CS has a very narrow distribution of the uncertainties compared to IM and MC which have broader distributions. MC has the broadest distribution and the most overprediction of the RMS error.

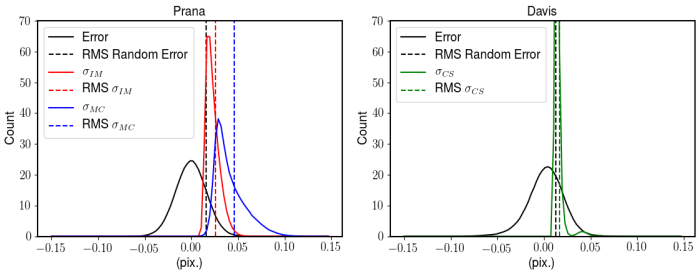

(a) (b)

Figure 5. Probability density functions (PDF) of the error and uncertainty distributions along with the corresponding RMS values. (a) Prana, IM and MC, (b) Davis, CS

The displacement fields were also used to calculate the projected density gradient fields using Equation (1), and spatially integrated using the Poisson solver to obtain the projected density field. The thickness of the density gradients from the simulation was then used to calculate the depth averaged density field. Dirichlet boundary conditions were imposed for the density integration procedure, and the density at all four boundaries was set to be values from the true density field used to render the images. Sample results of the depth-averaged density gradient and density fields are shown in .

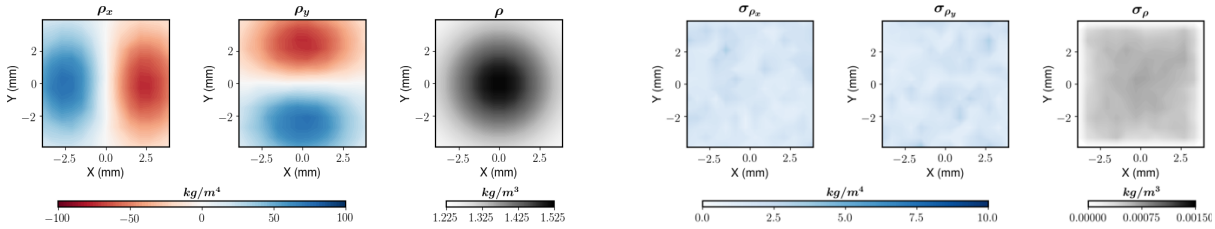

(a) **(b)**

Figure 6. Sample instantaneous depth-averaged (a) density gradients and density fields and (b) associated uncertainties obtained from the Poisson solver for Prana processing.

In addition, the displacement uncertainties from the cross-correlation analysis from each scheme were propagated through the Poisson solver to calculate the density uncertainties. Dirichlet boundary conditions were also used for the uncertainty propagation procedure, with the boundary uncertainties on the four sides set to be 0 ($\sigma_\rho = 0\ kg/m^3$). Sample instantaneous uncertainties in the depth-averaged density gradient and density fields are shown in .

The calculated density field was then compared with the original density field used to render the synthetic images and the density error was calculated. The resulting density errors from all thousand images were used to calculate error statistics. The density error statistics and the corresponding ensemble averaged density uncertainties are shown in for results from Prana, IM and MC, and in for results from Davis and CS.

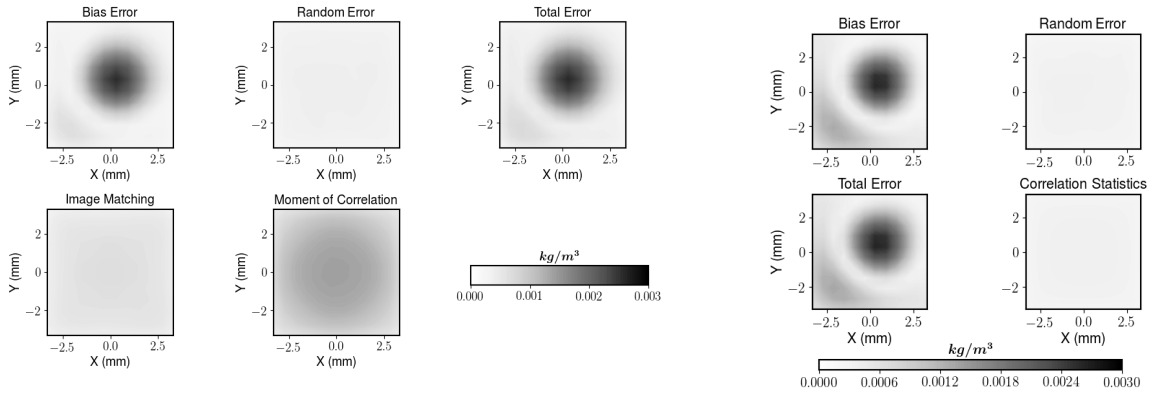

(a) (b)

Figure 7. Spatial variation of density error statistics for results along with the spatial variation of density uncertainties from (a) Prana, IM, MC and (b) Davis, CS processing.

From the figures it can be seen that unlike the displacement error statistics, the density error statistics show a strong bias error component, and hence the comparison should be performed between the random error and the uncertainty prediction. The density uncertainty predictions however are still spatially uniform for both CS and IM, while for MC, the density uncertainty overpredicts in a similar fashion to the displacement uncertainty results, with most of the over-prediction increasing towards the center. But overall, the density uncertainties are seen to be very small likely due to the uncertainty being set to zero at the boundaries.

The PDFs of the density error and uncertainty distributions is shown in Figure 8 (a) for Prana-IM-MC and in Figure 8 (b) for Davis-CS, along with the corresponding RMS values. Due to the strong bias error in the density results, the RMS of the *random error* will be compared to the RMS of the density uncertainty distributions, and a closer match signifies a better performance. As in the displacement uncertainty results, it is again seen that CS gives the best match between the RMS of the random error and the uncertainty, followed by IM and MC. It is also interesting to note that unlike the displacement error PDFs, the density error PDFs are non-Gaussian, and skewed towards the negative values, signifying that the density error is primarily due to under-prediction. The skewness of the error distribution is also consistent with the strong bias error seen in the spatial error maps in and .

(a) (b)

Figure 8. PDFs of the error and uncertainty distributions for (a) Prana error, IM, and MC uncertainty, and (b) Davis error and CS uncertainty.

Overall, it is seen from the analysis that (1) PIV based direct displacement uncertainty schemes are also applicable for BOS images, and (2) Correlation Statistics (CS) performs the best in both the displacement and density uncertainty prediction, though the density results showed a strong anisotropic bias error.

4. Analysis with Experimental Images

The uncertainty quantification methodology was also tested with experimental BOS images taken in a supersonic wind tunnel for Mach 2.5 flow over a 11.5° wedge with a base of 1 cm and a height of 2.5 cm. The dot pattern consisted of 0.15 mm diameter dots (corresponding to an image diameter of about 4 pix.) randomly distributed on a transparency with about 25 dots per 32x32 pix. window, and was back-illuminated using an LED with a diffuser plate to obtain uniform illumination. The dot pattern was imaged through the flow with a Photron SAZ camera and a Nikon 105 mm lens at a magnification of 55 um/pix. and an f-number of 32. The images were recorded at 1 kHz for a total of 3 seconds, at a total/stagnation pressure of 70 psia. A layout of the experimental setup is shown in Figure 9 (a), and the wedge geometry is shown in Figure 9 (b).

To account for the startup transients in the tunnel, only images corresponding to the last two seconds of each run are considered in the analysis. The duration of steady state operation of the tunnel was inferred from simultaneous 4 Hz pressure measurements from pressure taps located on the tunnel wall. To avoid masking based errors from affecting the analysis, only a small portion from the flow beneath the wedge is considered in this analysis, and a sample image of the dot pattern with the region of interest (ROI) is shown in Figure 9 (c).

The images were processed using the multi-pass window deformation approach described in the previous section for two passes with identical window sizes and overlap percentages (32x32 pix window size and 0% window overlap), with the intermediate pass validated and the final pass without validation. The images were processed using Prana with displacement uncertainty calculation from IM and MC, and using Davis with displacement uncertainty calculation from CS.

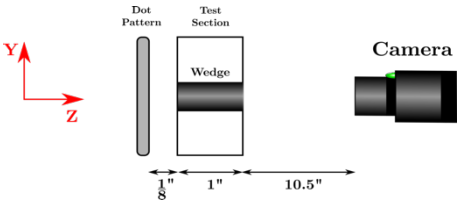

(a)

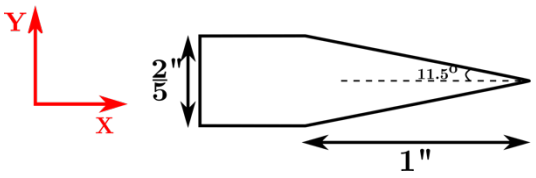

(b)

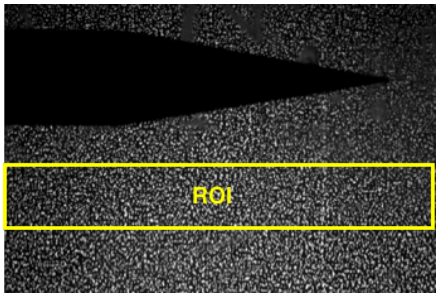

(c)

Figure 9. (a) Experimental layout, side view (b) schematic of the wedge, front view, (c) sample image with region of interest

The displacements were used to calculate the density gradients and density fields using the Poisson solver previously described. For the density integration, Dirichlet boundary conditions were used on the right boundary, where the density was set to be its free-stream value of 0.49 kg/m^3 and Neumann boundary conditions were imposed on the other three boundaries. Sample images of the path averaged density gradients and density fields are shown in Figure 10 for the two processing software programs, and it can be seen the gradients are highest in the regions corresponding to the shocks and expansion fans, but there are also non-zero density gradients ahead of and behind the shocks due to small stray displacements in these regions..

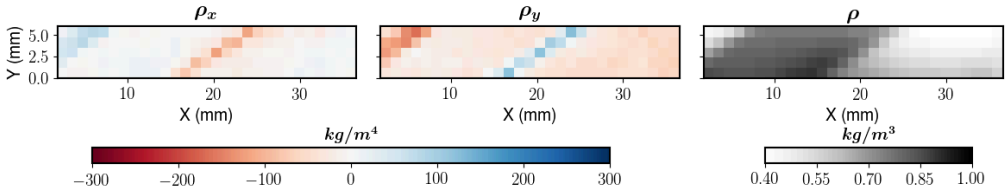

Figure 10. Sample density gradient and density fields from Pranaprocessing.

A similar approach was also followed for the uncertainty propagation, where a Dirichlet boundary condition was used on the right boundary with an uncertainty of 0.0 kg/m^3 and Neumann boundary conditions were imposed on the other three sides. Sample instantaneous uncertainties in the density gradient and density fields are shown in Figure 11.

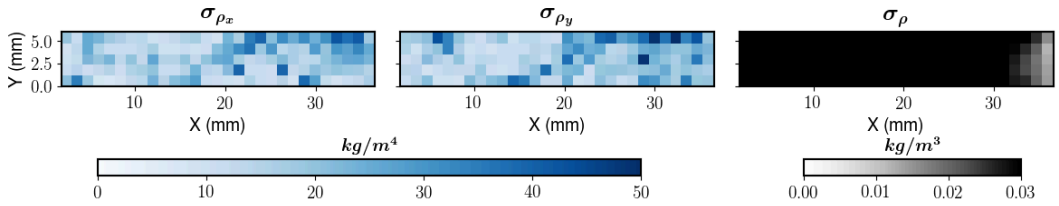

Figure 11. Sample instantaneous uncertainty fields for the density gradient and density from IM.

The true solution for the density was calculated from shock-expansion theory for inviscid compressible flow over a wedge (Anderson, 2004). First, the stagnation density was calculated by assuming an adiabatic compression of air from the atmosphere to the stagnation pressure in the reservoir. Using the known values of the atmospheric conditions (P_a=14.7 psi, $\rho_a = 1.225\ kg/m^3$), and the stagnation pressure ($P_0 = 70\ psia$), the stagnation density can be calculated. The free-stream density was calculated from the stagnation density and the Mach number using isentropic relations. The free-stream Mach number M_∞ was obtained from a combination of the pressure measurements along the nozzle wall, and by measuring the shock angle from a schlieren image. The density and Mach number in the region behind the shock are calculated using the oblique shock relations and are a function of the Mach number, the wedge angle, and the free-stream density. The density in the region behind the expansion is calculated using Prandtl-Meyer theory and is a function of the wedge shoulder angle (here equal to the wedge half angle 11°), as well as the post-shock Mach number and density. Finally, the theoretical solution is interpolated onto a regular grid corresponding to the vector locations from the cross-correlation, and, the density field obtained by integrating the displacement fields is compared with the theoretical density field to calculate the error.

The error distributions across two thousand images is used to calculate the error statistics, and the spatial distribution of the error statistics is shown in Figure 12 for Prana processing and Figure 13 for Davis processing, along with the ensemble averaged density uncertainties. Both processing software programs result in a large bias error (comparable to the random error), and all three uncertainty schemes massively underpredict their respective random errors. On further investigation, it was found that the wedge model deflects during the run, leading to changes in the flow field, and these changes could likely lead to the large random error.

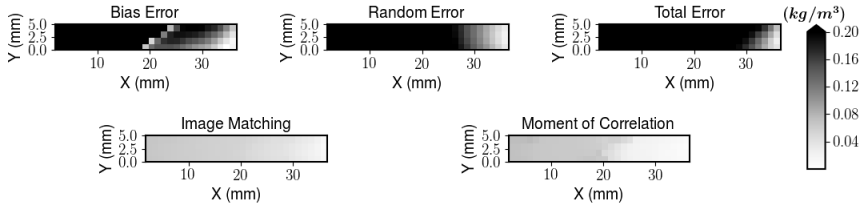

Figure 12. Spatial variation of error statistics from Prana processing and uncertainty predictions for Image Matching and Moment of Correlation schemes.

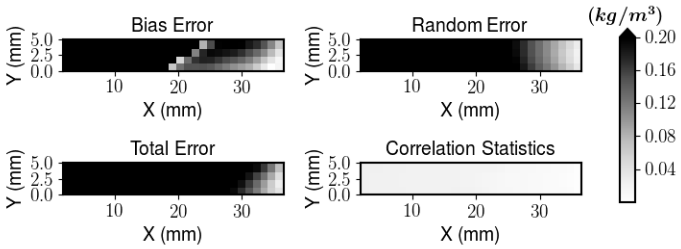

Figure 13. Spatial variation of errors statistics for Davis processing and uncertainty predictions for Correlation Statistics method.

Finally, the errors from all vectors in the time series are combined to calculate the PDFs for the error and uncertainty distributions, and are shown in Figure 14 along with the RMS values. The error PDF is very broad with heavy tails in comparison to the uncertainty PDFs, which are narrow and sharp. The density error pdf is also skewed towards the negative values, indicating an underprediction in the density measurements similar to the synthetic images, and the RMS of the random error is much higher (almost an order of magnitude) compared to the RMS of the uncertainties predicted by any of the schemes. This is most likely due to a limitation in the experiment as mentioned before, and efforts are ongoing in reducing the model vibrations during the run.

(a) (b)

Figure 14. PDFs of the error and uncertainty distributions for (a) Prana error, IM, and MC uncertainty, and (b) Davis error and CS uncertainty.

5. Conclusion

We have implemented and presented the first comprehensive uncertainty quantification framework for density estimation from BOS measurements and tested the method with synthetic and experimental BOS images. The methodology builds upon recent progress in a-posteriori uncertainty quantification in PIV, and the direct displacement uncertainty methods are used to also estimate the displacement uncertainty from BOS images. These displacement uncertainties are then propagated to the density gradients using the optical layout and then through the Poisson solver typically used for density integration in BOS to calculate density uncertainties, accounting for the covariances introduced due to the finite differences involved in the calculation of the Laplacian. This method yields, instantaneous, local, uncertainty bounds for each density measurement throughout the field of view.

The methodology was tested with synthetic BOS images rendered with a Gaussian density field using a ray-tracing based image generation methodology. The images were processed using correlation algorithms with multi-pass window deformation, and the errors were calculated by comparing the measured displacements to the light ray displacements, which are considered to be the ground truth. Processing was done on two different software programs, Prana and Davis, and three displacement schemes were used – Image Matching (IM), Moment of Correlation (MC) and Correlation Statistics (CS). Results show that for the displacements, all methods overpredict the true random error, with CS closest to the random error, followed by IM and MC.

When propagated through the Poisson solver for density integration, results both processing software programs resulted in a stronger bias error in the density field, likely due to truncation errors from the finite differences used in the density integration process. On comparing the random errors with the predicted density uncertainties, CS predicted a density uncertainty almost identical with the corresponding random error. IM and MC both overpredicted their respective random errors, but IM was closer to the true random error compared to MC.

The method was also tested on experimental BOS images of supersonic flow over a wedge and the processed displacements and the density fields show the presence of shocks and expansion fans in the region of interest corresponding to the wedge tip and wedge shoulder respectively. The density fields were compared with the theoretical solution from shock-expansion theory, and the error was calculated in the density measurement across two thousand fields to calculate error and uncertainty statistics. The results showed that all uncertainty schemes underpredict the density error by a large value, almost an order of magnitude. The reason for this error was found to be due to vibrations of the model in the wind tunnel which caused fluctuations in the density field. Efforts are ongoing to obtain new experimental data with a better fixture for the model in the tunnel.

Overall, it appears that displacement uncertainty methods typically used for PIV experiments are also equally applicable to BOS data, and the displacement uncertainties can be propagated through the Poisson solver using a sparse linear operator to obtain the density uncertainties. Thus, the method proposed in this manuscript allows for uncertainty quantification in density estimates from BOS measurements.

Acknowledgements

This material is based upon work supported by the U.S. Department of Energy, Office of Science, Office of Fusion Energy Sciences under Award Number DE-SC0018156.

References

Adrian, R. J. (2005). Twenty years of particle image velocimetry. *Experiments in Fluids*, *39*(2), 159–169. https://doi.org/10.1007/s00348-005-0991-7

Adrian, R. J., & Westerweel, J. (2011). *Particle image velocimetry*. Cambridge University Press.

Anderson, J. D. (2004). *Fundamentals of Aerodynamics* (4th ed.). McGraw-Hill.

Azijli, I., Sciacchitano, A., Ragni, D., Palha, A., & Dwight, R. P. (2016). A posteriori uncertainty quantification of PIV-based pressure data. *Experiments in Fluids*, *57*(5), 72. https://doi.org/10.1007/s00348-016-2159-z

Bhattacharya, S., Charonko, J. J., & Vlachos, P. P. (2017). Stereo-particle image velocimetry uncertainty quantification. *Measurement Science and Technology*, *28*(1), 015301. https://doi.org/10.1088/1361-6501/28/1/015301

Bhattacharya, S., Charonko, J. J., & Vlachos, P. P. (2018). Particle image velocimetry (PIV) uncertainty quantification using moment of correlation (MC) plane. *Measurement Science and Technology*, *29*(11). https://doi.org/10.1088/1361-6501/aadfb4

Boomsma, A., Bhattacharya, S., Troolin, D., Pothos, S., & Vlachos, P. P. (2016). A comparative experimental evaluation of uncertainty estimation methods for two-component PIV. *Measurement Science and Technology*, *27*(9). https://doi.org/10.1088/0957-0233/27/9/094006

Charonko, J. J., & Vlachos, P. P. (2013). Estimation of uncertainty bounds for individual particle image velocimetry measurements from cross-correlation peak ratio. *Measurement Science and Technology*, *24*(6). https://doi.org/10.1088/0957-0233/24/6/065301

Christensen, K. T., & Scarano, F. (2015). Uncertainty quantification in particle image velocimetry. *Measurement Science and Technology*, *26*(7), 070201. https://doi.org/10.1088/0957-0233/26/7/070201

Coleman, H. W., & Steele, W. G. (2009). *Experimentation, Validation, and Uncertainty Analysis for Engineers*. Hoboken,New Jersey: John Wiley & Sons, Inc.

Dalziel, S. B., Hughes, G. O., & Sutherland, B. R. (2000). Whole-field density measurements by "synthetic schlieren." *Experiments in Fluids*, *28*(4), 322–335. https://doi.org/10.1007/s003480050391

Dasch, C. J. (1992). One-dimensional tomography: a comparison of Abel, onion-peeling, and filtered backprojection methods. *Applied Optics*, *31*, 1146–1152. https://doi.org/10.1364/AO.31.001146

Eckstein, A. C., Charonko, J., & Vlachos, P. P. (2008). Phase correlation processing for DPIV measurements. *Experiments in Fluids*, *45*(3), 485–500. https://doi.org/10.1007/s00348-008-0492-6

Eckstein, A. C., & Vlachos, P. P. (2009a). Assessment of advanced windowing techniques for digital particle image velocimetry (DPIV). *Measurement Science and Technology*, *20*(7), 075402. https://doi.org/10.1088/0957-0233/20/7/075402

Eckstein, A. C., & Vlachos, P. P. (2009b). Digital particle image velocimetry (DPIV) robust phase correlation. *Measurement Science and Technology*, *20*(5), 055401. https://doi.org/10.1088/0957-0233/20/5/055401

Elsinga, G. E., Van Oudheusden, B. W., Scarano, F., & Watt, D. W. (2004). Assessment and application of quantitative schlieren methods: Calibrated color schlieren and background oriented schlieren. *Experiments in Fluids*, *36*(2), 309–325. https://doi.org/10.1007/s00348-003-0724-8

Gui, L., & Wereley, S. T. (2002). A correlation-based continuous window-shift technique to reduce the peak-locking effect in digital PIV image evaluation. *Experiments in Fluids*, *32*(4), 506–517. https://doi.org/10.1007/s00348-001-0396-1

Kirmse, T., Agocs, J., Schröder, A., Schramm, M. J., Karl, S., & Hannemann, K. (2011). Application of particle image velocimetry and the background-oriented schlieren technique in the high-enthalpy shock tunnel Göttingen. *Shock Waves*, *21*(3), 233–241. https://doi.org/10.1007/s00193-011-0314-2

Kolhe, P. S., & Agrawal, A. K. (2009). Abel inversion of deflectometric data: comparison of accuracy and noise propagation of existing techniques. *Applied Optics*, *48*(20), 3894–3902. https://doi.org/10.1364/AO.48.003894

Meier, G. (2002). Computerized background-oriented schlieren. *Experiments in Fluids*, *33*(1), 181–187. https://doi.org/10.1007/s00348-002-0450-7

Mizukaki, T., Wakabayashi, K., Matsumura, T., & Nakayama, K. (2014). Background-oriented schlieren with natural background for quantitative visualization of open-air explosions. *Shock Waves*, *24*(1), 69–78. https://doi.org/10.1007/s00193-013-0465-4

Raffel, M. (2015). Background-oriented schlieren (BOS) techniques. *Experiments in Fluids*, *56*(3), 1–17. https://doi.org/10.1007/s00348-015-1927-5

Raffel, M., Richard, H., & Meier, G. E. A. (2000). On the applicability of background oriented optical tomography for large scale aerodynamic investigations. *Experiments in Fluids*, *28*(5), 477–481. https://doi.org/10.1007/s003480050408

Raffel, M., Willert, C. E., Wereley, S. T., & Kompenhans, J. (2013). *Particle image velocimetry: a practical guide*. Springer.

Rajendran, L. K., Bane, S. P. M., & Vlachos, P. P. (2018). Dot-Tracking Methodology for Background Oriented Schlieren (BOS). *ArXiv:1812.10870*. Retrieved from http://arxiv.org/abs/1812.10870

Rajendran, L. K., Bane, S. P. M., & Vlachos, P. P. (2019). PIV/BOS synthetic image generation in variable density environments for error analysis and experiment design. *Measurement Science and Technology*, 11–14. https://doi.org/10.1088/1361-6501/ab1ca8

Ramanah, D., Raghunath, S., Mee, D. J., Rösgen, T., & Jacobs, P. A. (2007). Background oriented schlieren for flow visualisation in hypersonic impulse facilities. *Shock Waves*, *17*(1–2), 65–70. https://doi.org/10.1007/s00193-007-0097-7

Richard, H., & Raffel, M. (2001). Principle and applications of the background oriented schlieren (BOS) method. *Measurement Science and Technology*, *12*(9), 1576–1585. https://doi.org/10.1088/0957-0233/12/9/325

Richard, H., Raffel, M., Rein, M., Kompenhans, J., & Meier, G. E. A. (2002). Demonstration of the applicability of a Background Oriented Schlieren (BOS) method. In *Laser Techniques for Fluid Mechanics* (pp. 145–156). Berlin, Heidelberg: Springer Berlin Heidelberg. https://doi.org/10.1007/978-3-662-08263-8_9

Scarano, F. (2002). Iterative image deformation methods in PIV. *Measurement Science and Technology*, *13*(1), R1–R19. https://doi.org/10.1088/0957-0233/13/1/201

Scarano, F., & Riethmuller, M. L. (1999). Iterative multigrid approach in PIV image processing with discrete window offset. *Experiments in Fluids*, *26*(6), 513–523. https://doi.org/10.1007/s003480050318

Scarano, F., & Riethmuller, M. L. (2000). Advances in iterative multigrid PIV image processing. *Experiments in Fluids*, *29*(7), S051–S060. https://doi.org/10.1007/s003480070007

Sciacchitano, A. (2019). Uncertainty quantification in particle image velocimetry. *Measurement Science and Technology*, 0–16. https://doi.org/10.1088/1361-6501/ab1db8

Sciacchitano, A., Neal, D. R., Smith, B. L., Warner, S. O., Vlachos, P. P., Wieneke, B., & Scarano, F. (2015). Collaborative framework for PIV uncertainty quantification: comparative assessment of methods. *Measurement Science and Technology*, *26*(7), 074004. https://doi.org/10.1088/0957-0233/26/7/074004

Sciacchitano, A., & Wieneke, B. (2016). PIV uncertainty propagation. *Measurement Science and Technology*, *27*(8), 084006. https://doi.org/10.1088/0957-0233/27/8/084006

Sciacchitano, A., Wieneke, B., & Scarano, F. (2013). PIV uncertainty quantification by image matching. *Measurement Science and Technology*, *24*(4), 045302. https://doi.org/10.1088/0957-0233/24/4/045302

Sibson, R. (1981). A brief description of natural neighbor interpolation. In V. Barnett (Ed.), *Interpolating Multivariate Data* (pp. 21–36). Chichester: John Wiley.

Singh, B., Rajendran, L. K., Gupta, P., Scalo, C., Vlachos, P. P., & Bane, S. P. M. (2019). Experimental and Numerical Study of Flow Induced by Nanosecond Repetitively Pulsed Discharges. *AIAA Scitech 2019 Forum*, (January), 1–15. https://doi.org/10.2514/6.2019-0740

Sommersel, O. K., Bjerketvedt, D., Christensen, S. O., Krest, O., & Vaagsaether, K. (2008). Application of background oriented schlieren for quantitative measurements of shock waves from explosions. In *Shock Waves* (Vol. 18, pp. 291–297). https://doi.org/10.1007/s00193-008-0142-1

Sourgen, F., Haertig, J., & Rey, C. (2004). Comparison Between Background Oriented Schlieren Measurements (BOS) and Numerical Simulations. *24th AIAA Aerodynamic Measurement Technology and Ground Testing Conference*, *2602*(July), 1–18. https://doi.org/10.2514/6.2004-2602

Timmins, B. H., Wilson, B. W., Smith, B. L., & Vlachos, P. P. (2012). A method for automatic estimation of instantaneous local uncertainty in particle image velocimetry measurements. *Experiments in Fluids*, *53*(4), 1133–1147. https://doi.org/10.1007/s00348-012-1341-1

Venkatakrishnan, L. (2005). Density Measurements in an Axisymmetric Underexpanded Jet by Background-Oriented Schlieren Technique. *AIAA Journal*, *43*(7), 1574–1579. https://doi.org/10.2514/1.12647

Venkatakrishnan, L., & Meier, G. E. a. (2004). Density measurements using the Background Oriented Schlieren technique. *Experiments in Fluids*, *37*(2), 237–247. https://doi.org/10.1007/s00348-004-0807-1

Venkatakrishnan, L., & Suriyanarayanan, P. (2009). Density field of supersonic separated flow past an afterbody nozzle using tomographic reconstruction of BOS data. *Experiments in Fluids*, *47*(3), 463–473. https://doi.org/10.1007/s00348-009-0676-8

Wernet, M. P. (2005). Symmetric phase only filtering: a new paradigm for DPIV data processing. *Measurement Science and Technology*, *16*(3), 601–618. https://doi.org/10.1088/0957-0233/16/3/001

Westerweel, J., Dabiri, D., & Gharib, M. (1997). The effect of a discrete window offset on the accuracy of cross-correlation analysis of digital PIV recordings. *Experiments in Fluids*, *23*(1), 20–28. https://doi.org/10.1007/s003480050082

Westerweel, J., Elsinga, G. E., & Adrian, R. J. (2013). Particle Image Velocimetry for Complex and Turbulent Flows. *Annual Review of Fluid Mechanics*, *45*(1), 409–436. https://doi.org/10.1146/annurev-fluid-120710-101204

Westerweel, J., & Scarano, F. (2005). Universal outlier detection for PIV data. *Experiments in Fluids*, *39*(6), 1096–1100. https://doi.org/10.1007/s00348-005-0016-6

Wieneke, B. (2015). PIV uncertainty quantification from correlation statistics. *Measurement Science and Technology*, *26*(7), 074002. https://doi.org/10.1088/0957-0233/26/7/074002

Wilson, B. M., & Smith, B. L. (2013). Uncertainty on PIV mean and fluctuating velocity due to bias and random errors. *Measurement Science and Technology*, *24*(3), 035302. https://doi.org/10.1088/0957-0233/24/3/035302

Xue, Z., Charonko, J. J., & Vlachos, P. P. (2014). Particle image velocimetry correlation signal-to-noise ratio metrics and measurement uncertainty quantification. *Measurement Science and Technology*, *25*(11), 115301. https://doi.org/10.1088/0957-0233/25/11/115301

Xue, Z., Charonko, J. J., & Vlachos, P. P. (2015). Particle image pattern mutual information and uncertainty estimation for particle image velocimetry. *Measurement Science and Technology*, *26*(7), 074001. https://doi.org/10.1088/0957-0233/26/7/074001